Materials Today Bio 23 (2023) 100828

Contents lists available at ScienceDirect

Materials Today Bio

journal homepage: www.journals.elsevier.com/materials-today-bio

Enhancing the sensitization of neuroblastoma to radiotherapy by the construction of a dual-channel parallel free radicals nanoamplifier

Wenxin Zhang [a], Xiaodie Li [b], Jialin Zeng [b], Xin Wen [c], Chao Zhang [b], Yinan Zhang [d,**], Jian He [e,***], Lihua Yang [a,*]

[a] Department of Pediatric Hematology, Zhujiang Hospital, Southern Medical University, Guangzhou, Guangdong, 510282, China
[b] Department of Oncology, Zhujiang Hospital, Southern Medical University, Guangzhou, Guangdong, 510282, China
[c] Clinical Research Centre, Zhujiang Hospital, Southern Medical University, Guangzhou, 510282, China
[d] School of Chemical Science and Engineering, Tongji University, Shanghai, 200092, China
[e] Department of Nuclear Medicine, Nanjing Drum Tower Hospital, The Affiliated Hospital of Nanjing University Medical School, Nanjing, 210008, China

ARTICLE INFO

Keywords:
Radiotherapy
Free radicals
Radiosensitization
Nanoparticles
Neuroblastoma

ABSTRACT

Radiation therapy (RT) has emerged as one of the most promising anti-tumor strategies for neuroblastoma. Nevertheless, the special tumor microenvironment (TME), including hypoxic and GSH-overexpressed TME, often greatly restricts the RT outcome. In this study, we demonstrated a dual-channel parallel radicals nanoamplifier (ATO@PAE-PEG-AS1411/Fe^{3+}). The nanoamplifier was shaped into a bilayer shell-core structure, in which atovaquone-loaded poly (β-amino esters)-poly (ethylene glycol) (ATO@PAE-PEG) served as the core while Fe^{3+}-absorbed AS1411 aptamer (AS1411/Fe^{3+}) served as the shell. Taking advantage of the targeting ability of AS1411, ATO@PAE-PEG-AS1411/Fe^{3+} specifically accumulated in tumor cells, and then released ATO as well as Fe^{3+} in response to the acidic TME. The released ATO dramatically inhibited the mitochondrial respiration of tumor cells, thus sparing vast amounts of oxygen for the generation of free radicals during RT process, which was the first free radicals-amplifying pathway Meanwhile, the released Fe^{3+} could consume the tumor-overexpressed GSH through the redox reaction, thus effectively preserving the generated free radicals in RT process, which was the second free radicals-amplifying pathway. Taken together, our study demonstrates a dual-channel parallel free radicals-amplifying RT strategy, and it is expected this work will promote the clinical application prospects of RT treatment against neuroblastoma.

1. Introduction

Neuroblastoma is the most frequent extracranial solid tumor of childhood [1], typically diagnosed around 2 years of age [2] and responsible for 15% of childhood cancer-related deaths [3,4]. Primary neuroblastomas originate from cells of the sympathetic nervous system in the adrenal medulla or along the sympathetic chain, and clinical symptoms vary depending on the site of tumors, such as abdominal mass, abdominal pain, respiratory distress, or neurological symptoms from spinal cord participation [5]. Besides the location of primary tumors, patients are divided into low-risk group or high-risk group according to other factors including age, histology and molecular typing of tumors [6]. Therapy is stage- and risk-stratified, yet the survival rate in patients regarding as high risk is still lower than 50% with the use of surgery and chemotherapy in major [3,5]. Besides, radiation therapy (RT) is one of the crucial medical treatments to neuroblastomas with the

Abbreviations: RT, radiation therapy; TEM, tumor microenvironment; LDRT, low-dose radiation therapy; GSH, glutathione; PAE-PEG, poly (β-amino esters)-poly (ethylene glycol); ATO, atovaquone; GSSG, disulphide; ROS, oxygen free radicals; NHS, N-Hydroxysuccinimide; DMEM, Dulbecco's modified Eagle medium; PBS, phosphate-buffered saline; rDS, random DNA sequence; DTNB, 5,5′-Dithiobis (2-nitrobenzoic acid); EDC, 1-(3-Dimethylaminopropyl)-3-ethylcarbodiimide hydrochloride; DAPI, 4′,6-diamidino-2-phenylindole; FITC, fluorescein isothiocyanate; ICG, indocyanine green; CCK-8, Cell Counting Kit-8; HE, hematoxylin-eosin; TUNEL, terminal deoxynucleotidyl transferase dUTP nick end labeling.

* Corresponding author.
** Corresponding author.
*** Corresponding author.
E-mail addresses: yinan_zhang@tongji.edu.cn (Y. Zhang), hjxueren@126.com (J. He), dryanglihua@163.com (L. Yang).

https://doi.org/10.1016/j.mtbio.2023.100828
Received 5 August 2023; Received in revised form 13 September 2023; Accepted 1 October 2023
Available online 3 October 2023

utilization of radioactivity and x-rays [7], which is requisite for the patients perceived high-risk, especially indispensable for the cases where the tumor has metastatic spread and is not removable by the treatments of surgery or chemotherapy alone. In addition, it is routinely used in patients under life-threatening clinical symptoms and emergency to promptly scale down the size of tumor [8,9]. However, dose escalation is needed for the high-risk neuroblastoma [10,11], which means increasing risk of side effects including skin burns, hair loss, bone damage, and cardiovascular and respiratory problems [12]. Due to the high risk of side effects, high-dose RT should be avoided, but low-dose RT (LDRT) [13,14] can only achieve poor cancer treatment outcome.

To amplify the treatment outcome of LDRT, various radiosensitizers that can improve the sensitivity of tumor to radiation have been developed [15]. The mechanism of action behind RT is to induce DNA single strand breaks, DNA double strand breaks, or DNA and DNA cross-links through the production of oxygen free radicals (ROS) during the ionizing radiation process [16,17]. For this reason, oxygen free radicals-amplifying radiosensitizers that exert radiosensitization by the controllable generation of oxygen free radicals under external stimuli, such as laser irradiation, electric fields, or ultrasound, have been becoming more and more popular [18]. Though successful to some extent, the translation significance is still suffered from two limited aspects. On the one hand, the generation of oxygen free radicals is usually at the expense of the consumption of oxygen, which, however, cannot be afforded by tumor hypoxia microenvironment in neuroblastoma [19]. On the other hand, the highly-expressed reduced glutathione (GSH) in tumor cells, as an antioxidant in the tumor microenvironment, will reduce the generated free radicals, which greatly compromises the oxygen free radicals-amplifying radiosensitization [20]. As such, it is urgently desired to seek a special radiosensitizer that can reverse tumor hypoxia microenvironment and simultaneously can circumvent GSH-driven free radicals scavenging.

Common approaches to overcoming tumor hypoxia microenvironment is to improve tumor oxygenation by increasing oxygen delivery with Perfluorocarbons (PFCs) or Hemoglobin (Hb), catalyzing the decomposition of hydrogen peroxide (H_2O_2) with catalase or nanobiomimetic enzyme to produce oxygen in situ, reshaping tumor vessels with small molecular drugs or some angiogenesis inhibitors to improve the efficiency of oxygen diffusion to tumor cells, but they still suffer from several limitations [21–23]. Recently, mitochondrial respiratory inhibitors, such as atovaquone (ATO), has been reported that may effectively inhibit mitochondrial from consuming oxygen and radically overcome tumor hypoxia microenvironment [24–26]. In addition, it's demonstrated that oxidized metal ions such as Fe^{3+} and Cu^{2+} can reduce overexpressed GSH in tumor by oxidizing glutathione (GSH) into glutathione disulphide (GSSG), break the redox homeostasis in tumor, and destroy the antioxidant self-repair pathway to reduce oxidative damage [27].

In this study, we elaborately designed a free radicals nanoamplifier (ATO@PAE-PEG-AS1411/Fe^{3+}, abbreviated A@P–P-AS/Fe^{3+}) for enhancing the sensitization of neuroblastoma to radiotherapy by two parallel pathways. The synthesis process and the mechanism behind the radiosensitization are displayed in Fig. 1. In detail, the core was constructed by the encasement of ATO into amphiphilic polymer poly (β-amino esters)-poly (ethylene glycol) (PAE-PEG) with superior biocompatibility and ability to disassemble in response to the tumor acidic microenvironment [28]. At the same time, the shell was self-assembled with AS1411, a DNA aptamer with high specific binding affinity to nucleolin on the surface of tumor cell membranes [29,30], and Fe^{3+} by the electrostatic force. The shell was then covalently

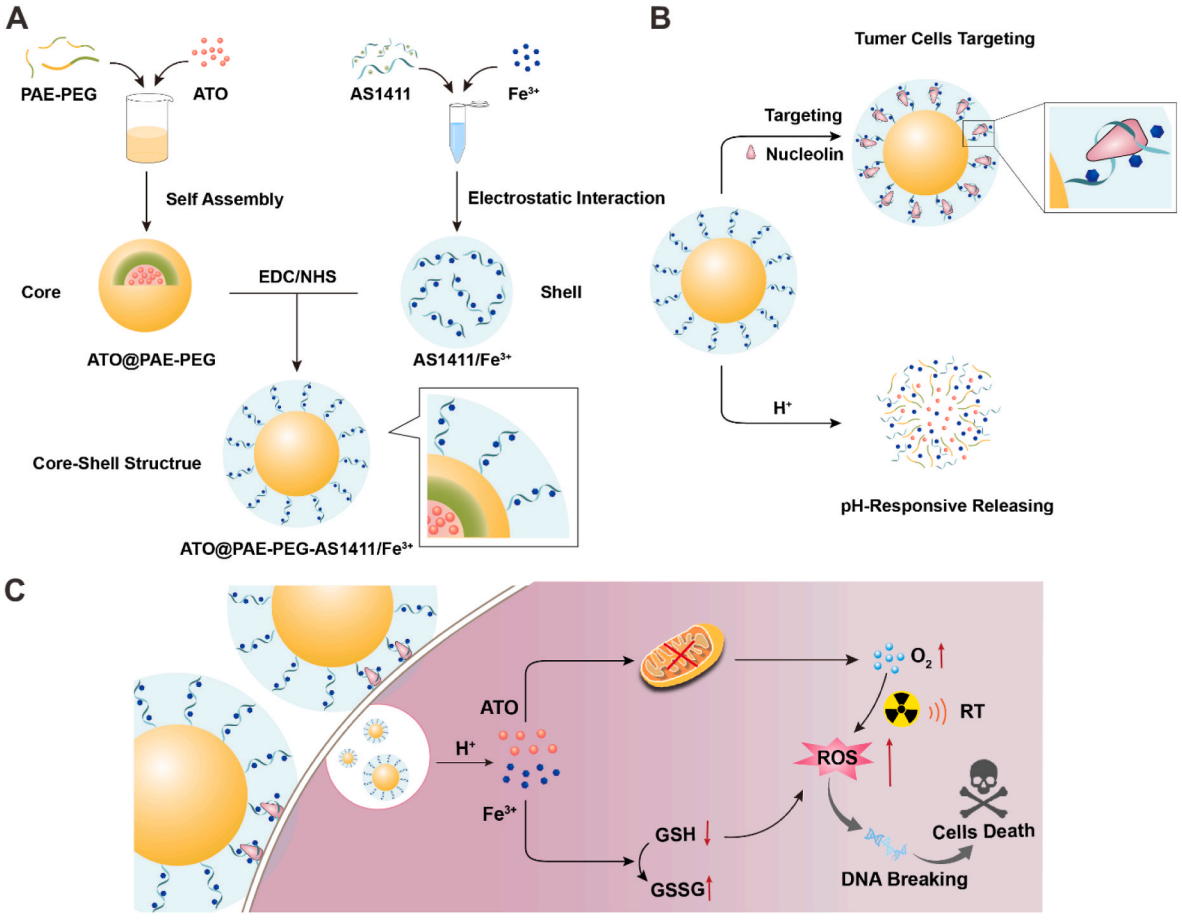

Fig. 1. Schematic illustration of synthesis and working principle of A@P–P-AS/Fe^{3+}.

modified onto the surface of the core to develop a novel bilayer shell-core radicals nanoamplifier A@P–P-AS/Fe^{3+} (Fig. 1A). With the capabilities of tumor cells targeting and pH-responsive releasing, A@P–P-AS/Fe^{3+} massively accumulated in the tumor cells, and then released ATO and Fe^{3+}. ATO as mitochondrial respiratory inhibitor, limited oxygen consumption in situ, which provided more oxygen for the generation of ROS. Meanwhile, Fe^{3+} oxidized GSH into GSSH, disrupting the redox homeostasis in the tumor cells and preserving more ROS from being scavenging (Fig. 1B and C). Consequently, these dual-channel parallel free radicals-amplifying pathways dramatically promoted the production of ROS by RT, making it possible to boost the low dose RT outcome. We expect this platform to yield a clinical breakthrough against the high-risk neuroblastoma.

2. Material and methods

2.1. Material

The poly (β-amino esters)-poly (ethylene glycol) with carboxyl modified on the terminals (PAE-PEG-COOH) were purchased from Xi'an ruixi Biological Technology. AS1411 aptamer with amine modified on the terminals (5′-GGTGGTGGTGGTTGTGGTGGTGGTGG-NH_2-3′) and random DNA sequence as many bases as AS1411 was synthesized by Shanghai Sangon Biotech. Iron chloride hexahydrate ($FeCl_3{\cdot}6H_2O$), dichloromethane (CH_2Cl_2), Dulbecco's modified Eagle medium (DMEM), N-Hydroxysuccinimide (NHS), phosphate buffer (PBS), 5,5′-Dithiobis (2-nitrobenzoic acid) (DTNB) and 1-(3-Dimethylaminopropyl)-3-ethylcarbodiimide hydrochloride (EDC) were all provided by Procell (Wuhan, China). Membrane Protein Extraction Kit was obtained from Ab-mart. Reactive oxygen species assay kit, Cell Counting Kit-8, Live/Dead Viability Assay Kit, Annexin V-FITC/PI Apoptosis Detection Kit, JC-1 Dye (Mitochondrial Membrane Potential Probe) were all purchased from Aladdin Reagent (Shanghai, China) and Hypoxyprobe kit (BestBio, Shanghai, China). Neuroblastoma SK-N-BE (2) cells line was acquired from Procell (Wuhan, China). Lipid Peroxidation MDA Assay Kit, Colorimetric TUNEL Apoptosis Assay Kit and anti-Ki67 antibody and anti-γ-H2AX antibody were both purchased from Beyotime (China). Radiation therapy was performed by Benchtop X-Ray Irradiator (Cellrad, American).

2.2. Synthesis of A@P–P-AS/Fe^{3+}

Firstly, 10 mg ATO was dissolved in 5 mL dichloromethane. Then, the solution was quickly poured into 50 mL ultrapure water dissolved with 50 mg PAE-PEG. After being stirred for 1–2 min, the mixed suspension was emulsified by ultrasonic emulsification for 30–60 min until the dichloromethane was completely evaporated, and ATO@PAE-PEG (abbreviated A@P–P) polymerized microspheres were obtained after repeated centrifugation (10,000 r/min, 10 min) and cleaning for 3 times. The AS1411 powder and $FeCl_3{\cdot}6H_2O$ were respectively dissolved in enzyme-free solution and configured to the specification of 5 mL/1 μM and 5 mL/100 μM, then the solution involving Fe^{3+} was added to the solution of AS1411 drop by drop, stirred continuously at room temperature for 24 h as the positively charged Fe^{3+} and the negatively charged phosphate skeleton of AS1411 self-assembled together via electrostatic force. Then, the solution was placed in the ultrafiltration tube (retention MW 3 kD), centrifuged (10,000 r/min, 10 min) and rinsed with ultrapure water for 3 times. After that, the shell, that is, AS1411/Fe^{3+} (abbreviated AS/Fe^{3+}) was obtained. 50 mg A@P–P nanospheres and 50 mg EDC were placed in the 50 mL pH 7.0 solution of PBS, stirred for 10 min, then 30 mg NHS was added into the solution, after reacting for 2–6 h, the activation of the carboxyl group on the PEG of A@P–P was completed. After centrifugation (10,000 r/min, 10 min) and cleaning for 3 times, carboxyl-activated A@P–P was dissolved in the 50 mL pH 7.8 solution of PBS, reacted with excessive AS/Fe^{3+} for 4–6 h. Then, the solution was put into the ultrafiltration tube (retention MW 100 kD), and centrifuged under 10,000 r/min by ultracentrifugation for 10 min. After the centrifugation and cleaning for 3 times, ATO@PAE-PEG-AS1411/Fe^{3+} (abbreviated A@P–P-AS/Fe^{3+}) was finally obtained.

2.3. Characterization of A@P–P-AS/Fe^{3+}

The morphology of the A@P–P, AS/Fe^{3+} and A@P–P-AS/Fe^{3+} were observed by transmission electron microscopy (TEM) (Thermo Scientific Talos F200i S/TEM). Zeta-potential value and the size distribution was tested by Particle Size Analyzers (Litesizer™ 500, Anton Paar). The UV–vis absorption spectra of the ATO, PEG-PAE and A@P–P was tested on spectrophotometer (Mettler, UV5Nano). Scanning electron microscope (SEM) and energy dispersive spectrometer (EDS) was used to observe A@P–P-AS/Fe^{3+} and the elements distribution. FTIR spectra of A@P–P-AS/Fe^{3+} was detected by thermofisher IS20 nicolet. The plasma stability of A@P–P-AS/Fe^{3+} during 7 days was monitored by its diameters. The Fe and P element content in the AS/Fe^{3+}, A@P–P and A@P–P-AS/Fe^{3+} was detected by Agilent 7850 ICP-MS. The encapsulation efficiency and loading content of ATO and Fe^{3+} in A@P–P-AS/Fe^{3+} was estimated by High-performance liquid chromatography (HPLC, Agilent Technologies-1200) and Inductively Coupled Plasma Mass Spectrometry (ICP-MS, Agilent-7850). The encapsulation efficiency and loading content were calculated by following formulas:

$$\text{Encapsulation efficiency}\ (\%) = \frac{\text{Weight of the feeding drug}_{-\text{Weight of the free drug}}}{\text{Weight of the feeding drug}} \times 100\%$$

$$\text{Loading content}\ (\%) = \frac{\text{Weight of the feeding drug} - \text{Weight of the free drug}}{\text{Weight of the NPs}} \times 100\%$$

2.4. In vitro cellular uptake

To evaluate the capacity of the A@P–P-AS/Fe^{3+} to target tumor cells, firstly, Indocyanine Green (ICG, Ex/Em = 785/810 nm) was packaged together with ATO into PAE-PEG microspheres to visualize the nanoamplifier (ICG-A@P–P-AS/Fe^{3+}). SK-N-BE (2) cells were seeded in the confocal dish (2×10^6 cells/well) at 37 °C for 24 h. Then, The SK-N-BE (2) cells were subsequently in co-culture with PBS (control), ICG-A@P–P-rDS/Fe^{3+} (rDS: random DNA sequence as many base as AS1411, but without targeting ability) (5 μg/mL), ICG-A@P–P-AS (without Fe^{3+}) (5 μg/mL) and ICG-A@P–P-AS/Fe^{3+} (5 μg/mL) for 6 h at 37 °C, followed by incubation with DAPI (10 μg/mL, Ex/Em = 364/454 nm) and FITC-Phalloidin (100 nM, Ex/Em = 545/570 nm) at 25 °C for 30 min, and then cleaned by PBS twice. After that, the SK-N-BE (2) cells were observed by confocal laser scanning microscopy. The treated cells were then collected for Flow Cytometry. The expression of nucleolin (AS1411 targeting protein) on the membrane of SK-N-BE (2) cells was detected by Western Blot (the protein was purified using a Membrane Protein Extraction Kit, Ab-mart, #A1008).

2.5. pH-responsive releasing assay

To assess the performance of A@P–P-AS/Fe^{3+} pH-responsive releasing, the nanoparticles (NPs) were placed into neutral PBS (pH 7.4) or acidic PBS (pH 5.0) respectively for 48 h, and Particle Size Analyzers was used to monitor the hydration particle size of A@P–P-AS/Fe^{3+} per 5 h. Besides, the accumulative release of ATO and Fe^{3+} was detected by High-performance liquid chromatography (HPLC, Thermo Fisher Scientific) and Inductively Coupled Plasma Mass Spectrometry (ICP-MS, Thermo Fisher Scientific).

2.6. Detection of hypoxia

To investigate whether A@P–P-AS/Fe^{3+} would inhibit mitochondrial from consuming oxygen and radically overcome tumor hypoxia microenvironment, Briefly, the SK-N-BE (2) cells were incubated on the 6-well plates (2×10^6 cells/well) at 37 °C for 24 h, then were subsequently incubated with PBS, ATO (5 μg/mL) and A@P–P-AS/Fe^{3+} (5 μg/mL) at 37 °C for another 24 h. In order to avert oxygen exchanging, liquid paraffin was placed onto the medium before the co-culture with PBS, ATO or A@P–P-AS/Fe^{3+}. After that, the SK-N-BE (2) cells were co-incubation with BBoxiProbe®RU $(DPP)_3Cl_2$ (100–200 μM, Ex/Em = 455/613 nm) at 37 °C for 30 min, followed by cleaned with PBS twice and were observed by the Nikon ECLIPSE Ti2 inverted microscope. At the same time, mitochondrial membrane potential of the SK-N-BE (2) cells after different treatments as above was detected by JC-1.

2.7. Detection of GSH

To investigate whether A@P–P-AS/Fe^{3+} would reduce overexpressed GSH in tumor cells, firstly, the SK-N-BE (2) cells were seeded in the 6-well plates (2×10^6 cells/well) at 37 °C for 24 h and then were subsequently incubated with PBS, Fe^{3+} (5 μg/mL) and A@P–P-AS/Fe^{3+} (5 μg/mL) at 37 °C for 6 h, with or without LDRT (1.5 Gy/10 min per 12 h, 3 Gy in total [13]). After that, the SK-N-BE (2) cells were cleaned by PBS and then collected into a centrifuge tube. Soon afterwards, the SK-N-BE (2) cells were lysed for 20 min with RIPA lysis and extraction buffer and centrifuged for 10 min (1000*g*, 4 °C). Finally, 50 μL of the supernatant was mixed with 100 μL DTNB (100 μM) for 1 h, and then the absorbance was recorded with microplate reader at 412 nm.

2.8. Detection of ROS

To investigate whether A@P–P-AS/Fe^{3+} would promote ROS accumulation during LDRT treatment, the SK-N-BE (2) cells were seeded in the 6-well plates (2×10^6 cells/well) at 37 °C for 24 h and then were subsequently incubated with PBS, ATO (5 μg/mL), Fe^{3+} (5 μg/mL), A@P–P (5 μg/mL), AS/Fe^{3+} (5 μg/mL) and A@P–P-AS/Fe^{3+} (5 μg/mL) for 6 h, with or without LDRT (1.5 Gy/10 min per 12 h, 3 Gy in total). After that, the cells were washed with PBS and then were incubated with the DCFH-DA probe (10 mM, Ex/Em = 488/525 nm) for 15 min at room temperature, followed by washed with PBS twice and then were observed by the Nikon ECLIPSE Ti2 inverted microscope.

2.9. In vitro synergistic cytotoxicity with or without LDRT

To evaluate whether A@P–P-AS/Fe^{3+} would amplify the radiosensitization on the SK-N-BE (2) cells, promote the apoptosis of them and improve the anticancer effect of LDRT, CCK-8 Assay, Live/Dead Cell Assay and Flow cytometry analysis were performed.

For CCK-8 assay: The SK-N-BE (2) cells were plated in 96-well plate (5×10^4 cells/well) at 37 °C for 24 h and then treated with PBS, ATO (5 μg/mL), Fe^{3+} (5 μg/mL), A@P–P (5 μg/mL), AS/Fe^{3+} (5 μg/mL) and A@P–P-AS/Fe^{3+} (5 μg/mL) at 37 °C for another 24 h, with or without LDRT (1.5 Gy/10 min per 12 h, 3 Gy in total). Wells without cells were considered as the blank-control. After incubation with different treatments, the cells in each well were incubated for more 4 h with 10 μL CCK-8 solution. Optical density (OD) at 450 nm was detected by microplate reader. Cell viability (%) was determined as

$$\text{Cell viability } (\%) = \frac{OD_{treatment} - OD_{blank}}{OD_{PBS} - OD_{blank}} \times 100\%$$

For Live/Dead Cell assay: The SK-N-BE (2) cells were plated in 6-well plate (5×10^6 cells/well) for at 37 °C 24 h and then incubated with PBS, A@P–P (5 μg/mL), AS/Fe^{3+} (5 μg/mL) and A@P–P-AS/Fe^{3+} (5 μg/mL) at 37 °C for 24 h, with or without LDRT (1.5 Gy/10 min per 12 h, 3 Gy in total). After that, the SK-N-BE (2) cells were cleaned with PBS and then were co-incubated with Nuclei Dye (Ex/Em = 535/617) and Live Dye (Ex/Em = 488/530 nm) at 37 °C for 30 min, followed by washed with PBS twice and then were observed by the Nikon ECLIPSE Ti2 inverted microscope.

For flow cytometry analysis: The SK-N-BE (2) cells were plated in 6-well plate (5×10^6 cells/well) and incubated for 24 h, followed by incubated with PBS or A@P–P-AS/Fe^{3+} (5 μg/mL) at 37 °C for 24 h, with or without LDRT (1.5 Gy/10 min per 12 h, 3 Gy in total). The SK-N-BE (2) cells were then collected into a centrifuge tube, resuspended with 500 μL binding buffer, and then stained with PI and Annexin V-FITC. After 20 min, data were obtained using CytoFLEX flow cytometer (Beckman).

2.10. Animals and tumor models

For in vivo studies, BALB/c mice (female, 4–5 weeks, 16–18 g) were obtained from Guangdong Medical Laboratory Animal Center (Guangdong, China). All animals were cared and treated according to the Institutional Animal Care and Use Committee (IACUC) of Southern Medical University (approval reference number: LAEC-2022-210). All animal experiments were implemented by the ratification of the Administration Committee of Experimental Animals in Guangdong Province and the Ethics Committee of Southern Medical University. Tumor models were established in BALB/c mice by subcutaneously implanting 1×10^7 SK-N-BE (2) cells suspended in 100 μL of PBS into the left and lower flank of the mice. Treatments were initiated when the tumor volumes reached approximately 150 mm^3.

2.11. Hemolysis assay

Each 96-well plate was added into 25 μL fresh mice red blood cells, 375 μL PBS and 100 μL A@P–P-AS/Fe^{3+} of different concentration, co-incubated at 37 °C for 1 h. Positive control: cellular lysate with mice red blood cells; negative control: PBS with mice red blood cells. After centrifugation at 3000 rpm for 5 min, the absorbance of the supernatants at 450 nm was detected. The relative percentage of hemolysis value was calculated by comparing it with the positive control.

2.12. Blood half-life detection

The SK-N-BE (2) subcutaneous tumors were developed in the mice above. To evaluate the blood half-life of the A@P–P-AS/Fe^{3+}, Tumor-bearing mice were intravenously injected with ICG-A@P–P-AS/Fe^{3+} (5 mg/kg). Mice were sacrificed, and blood was harvested at different time post-injection. Fluorescence data detected by Fluorescence detector (HPLC, Shimadzu) was normalized and presented as percentage of dose/g (% ID).

2.13. In vivo antitumor activity of A@P–P-AS/Fe^{3+} with or without LDRT

The SK-N-BE (2) subcutaneous tumors were developed in the mice above. To examine the targeting ability of A@P–P-AS/Fe^{3+} in vivo, ICG was packaged into the core, serving as the visualized marker of the nanoparticles. Tumor-bearing mice were intravenously injected with the groups of PBS + ICG (control), ICG-A@P–P-rDS/Fe^{3+} (rDS, random DNA sequence, without targeting ability), and ICG-A@P–P -AS/Fe^{3+} (AS, AS1411, with targeting ability) (0.5 mg/kg ICG for each group) and the fluorescence signal of ICG was investigated by the IVIS® Lumina III In Vivo Imaging System (PerkinElmer. America). After that, the tumor-bearing mice were divided as follows: group 1: PBS; group 2: PBS with LDRT (1.5 Gy/10 min per 12 h, 3 Gy in total); group 3: P–P-AS/Fe^{3+} (5 mg/kg); group 4: A@P–P-AS (5 mg/kg) with LDRT (1.5 Gy/10 min per 12 h, 3 Gy in total); group 5: A@P–P-AS/Fe^{3+} (5 mg/kg) with LDRT (1.5 Gy/10 min per 12 h, 3 Gy in total). The samples were given by intravenous injection via tail vein. The day of initial administration was set as

day 0 and 24 h after the injection, the tumors were exposed to LDRT (1.5 Gy/10 min per 12 h, 3 Gy in total). Tumor sizes and body weights were measured every two days for the duration of the test after the first treatment. At 24 h after treatment, tumors harvested from all groups above were stained by Hematoxylin-Eosin (HE), γ-H2AX, TUNEL and Ki-67. Besides, GSH level in tumor tissues was detected as the same method in vitro. Oxidative stress in tumor tissues after different treatments was detected using Lipid Peroxidation MDA Assay Kit (Beyotime, absorption wavelength: 532 nm). After two weeks of the treatment, the mice treated with different interventions were all sacrificed and the main organs (heart, spleen, liver, kidney and lung) were harvested for HE staining. The tumor volumes and tumor-restrained rate were calculated using the formulas below.

$$V_{tumor} = \frac{L_{tumor} \times W_{tumor}^2}{2}$$

$$R_{tumor-restrained} = \frac{V_{control} - V_{treatment}}{V_{control}} \times 100\%$$

2.14. Statistical analysis

The data in this article were analyzed by SPSS 22.0 Version (IBM Corporation, USA). Statistical analysis was performed by two-sided Student's t-test for two groups, and one-way ANOVA analysis of variance for multiple groups. The analyzed data were presented as mean ± SD, and each experiment was repeated at least three times. A value of $P < 0.05$ was considered statistically significant.

3. Results and discussion

3.1. Characterization of ATO@PAE-PEG-AS1411/Fe^{3+}

The observations by TEM (Fig. 2A) showed the morphology of the core ATO@PAE-PEG (abbreviated A@P–P). The encasement of ATO into A@P–P was verified given the fact that the characteristic absorption peak in UV–vis spectra of ATO (~297 nm) was successfully preserved in A@P–P (Fig. 2B). Combining with the TEM image of the shell AS1411/Fe^{3+} (abbreviated AS/Fe^{3+}) (Fig. S1), TEM image in Fig. 2C clearly reflected the bilayer shell-core structure of ATO@PAE-PEG-AS1411/Fe^{3+} (abbreviated A@P–P-AS/Fe^{3+}), with the surface shell of AS/Fe^{3+} and inner core of A@P–P. As shown in Fig. 2A and C, the resulting A@P–P-AS/Fe^{3+} had an average hydrodynamic diameter of 179.51 nm, 37.81 nm larger in diameter than that of the inner core A@P–P, and possessed a surface charge equivalent of 1.2 mV which was remarkably lower than that of A@P–P (8.6 mV) (Fig. 2D). To further verify whether AS/Fe^{3+} had been loaded, energy-dispersive X-ray spectroscopy (EDS) and ICP-MS were performed. EDS mapping clearly indicated the existence of Fe element in the A@P–P-AS/Fe^{3+} (Fig. 2E and F). Furthermore, the element content percentage of Fe and P is almost unchanged after

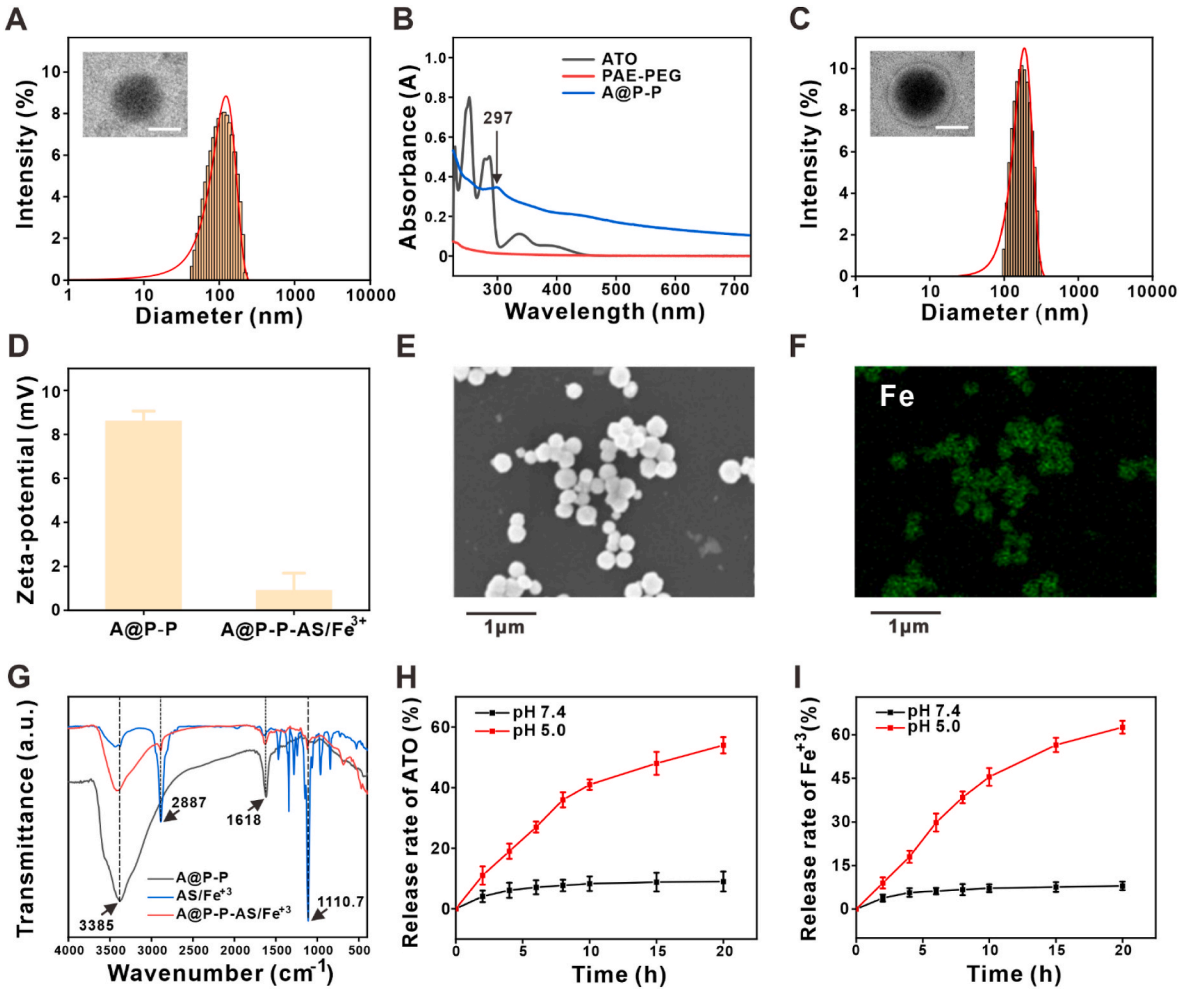

Fig. 2. Characterization of A@P–P-AS/Fe^{3+}. (A) Hydrodynamic diameter distribution of A@P–P (Inset: TEM image of A@P–P. Scale bar: 100 nm). (B) UV–vis spectra of ATO, PAE-PEG and A@P–P. (C) Hydrodynamic diameter distribution of A@P–P-AS/Fe^{3+} (Inset: TEM image of A@P–P-AS/Fe^{3+}. Scale bar: 100 nm). (D) Zeta potential diagram of A@P–P and A@P–P-AS/Fe^{3+} (n = 3). (E, F) SEM and EDS mapping (Fe element) images of A@P–P-AS/Fe^{3+}. Scale bar: 1 μm. (G) FTIR spectra of A@P–P, AS/Fe^{3+} and A@P–P-AS/Fe^{3+}. (H, I) The accumulative release percentage of ATO and Fe^{3+} during 20 h (n = 3).

AS1411/Fe^{3+} loaded on the ATO@PAE-PEG microspheres (from 16.85%:5.32%–4.67%:1.50%) (Fig. S2). Additionally, the FTIR spectra showed that the characteristic absorption peaks of A@P–P (3385 cm^{-1}, 1618 cm^{-1}) and AS/Fe^{3+} (2287 cm^{-1}, 1110.7 cm^{-1}) were successfully preserved in A@P–P-AS/Fe^{3+} (Fig. 2G). Therefore, we confirmed that the shell AS/Fe^{3+} had been loaded into the A@P–P-AS/Fe^{3+}. Encapsulation efficiency and loading content of ATO and Fe^{3+} in ATO@PAE-PEG-AS1411/Fe^{3+} could be found in Table S1. The results of size distribution of A@P–P-AS/Fe^{3+} in pH 7.4 or pH 5.0 during 20 h showed that the hydration particle size of A@P–P-AS/Fe^{3+} had no significant change under the condition of pH 7.4, while the hydration particle size of A@P–P-AS/Fe^{3+} decreased gradually under the condition of pH 5.0 (Fig. 3A). Combined with the TEM image (Fig. 3B), it was obvious that A@P–P-AS/Fe^{3+} disassembled under the condition of pH 5.0, and the fragments from the disassembly of A@P–P-AS/Fe^{3+} were clearly visible. Besides, we evaluated the plasma stability of A@P–P-AS/Fe^{3+} during 7 days by monitoring its diameter in contrast with PBS (Fig. S3). Moreover, as shown in Fig. 2H and I, the accumulative release of ATO and Fe^{3+} were significantly promoted at the condition of pH 5.0, with the results of 53.4% (ATO) and 62.6% (Fe^{3+}) after 20 h, which meant that A@P–P-AS/Fe^{3+} was capable of responding to the tumor acidic microenvironment and releasing encased ATO and Fe^{3+}.

To verify the DNA aptamer AS1411 would confer A@P–P-AS/Fe^{3+} with tumor-targeting potential, cellular uptake assay in vitro was performed. Before that, we have confirmed the expression of nucleolin on the membrane of SK-N-BE (2) cells (Fig. S4). To visualize the nanoparticles (NPs), ICG was packaged together with ATO into PAE-PEG microspheres as the label of the NPs. As shown in Fig. 3C, compared with the group of ICG-A@P–P-rDS/Fe^{3+} (rDS: random DNA sequence, without targeting ability), it revealed that the AS1411 (with targeting ability) may enhance the ability of ICG-A@P–P-AS/Fe^{3+} to undergo cellular uptake. In addition, in order to explore whether the expression of nucleolin on the membrane of SK-N-BE (2) tumor cells would influence the targeting ability of A@P–P-AS/Fe^{3+}, we treated the SK-N-BE (2) tumor cells with starvation treatment (in co-culture with serum-free medium) per previous report [31] to lower the expression of nucleolin. We confirmed that, compared with non-starved SK-N-BE (2) cells, the expression of nucleolin on the membrane of SK-N-BE (2) cells was exactly lowered after the starvation treatment (Fig. S4). As shown in Fig. S5, the cellular uptake of A@P–P-AS/Fe^{3+} obviously diminished in the starved SK-N-BE (2) cells in contrast to the non-starved group. The observations above indicated that the high specific binding affinity of AS1411 to the nucleolin on the surface of the tumor cells would help A@P–P-AS/Fe^{3+} actively target into the SK-N-BE (2) cells, and accumulate in cytoplasm. Furthermore, we proved that presence of Fe^{3+} in ATO@PAE-PEG-AS1411/Fe^{3+} would not obviously affect the targeting ability of AS1411 (Fig. S6).

3.2. *A@P–P-AS/Fe^{3+}-rendered dual-channel parallel ROS-generating pathway*

Previous reporting indicates that ATO may reduce oxygen consumption by blocking the electron transfer in respiratory chain which maintains the high-level mitochondria membrane potential [32]. The mitochondrial membrane potential after different treatments was assessed with the utilization of JC-1 dye. As shown in Fig. 4A, high-level mitochondrial membrane potential of untreated cells was reflected by the massive red fluorescence (JC-1 aggregates), whereas the green fluorescence (JC-1 monomers) which suggested the depolarized mitochondrial membrane was identified in cells treated with ATO or A@P–P-AS/Fe^{3+} [33]. To confirm the inhibition of oxygen consumption by A@P–P-AS/Fe^{3+}, liquid paraffin was added onto the medium before different treatments to the SK-N-BE (2) cells in order to avoid the influence of oxygen exchange. Contrasted with the control group, hypoxia degree of the A@P–P-AS/Fe^{3+} group is obviously lower, which meant the presence of A@P–P-AS/Fe^{3+} significantly retarded oxygen

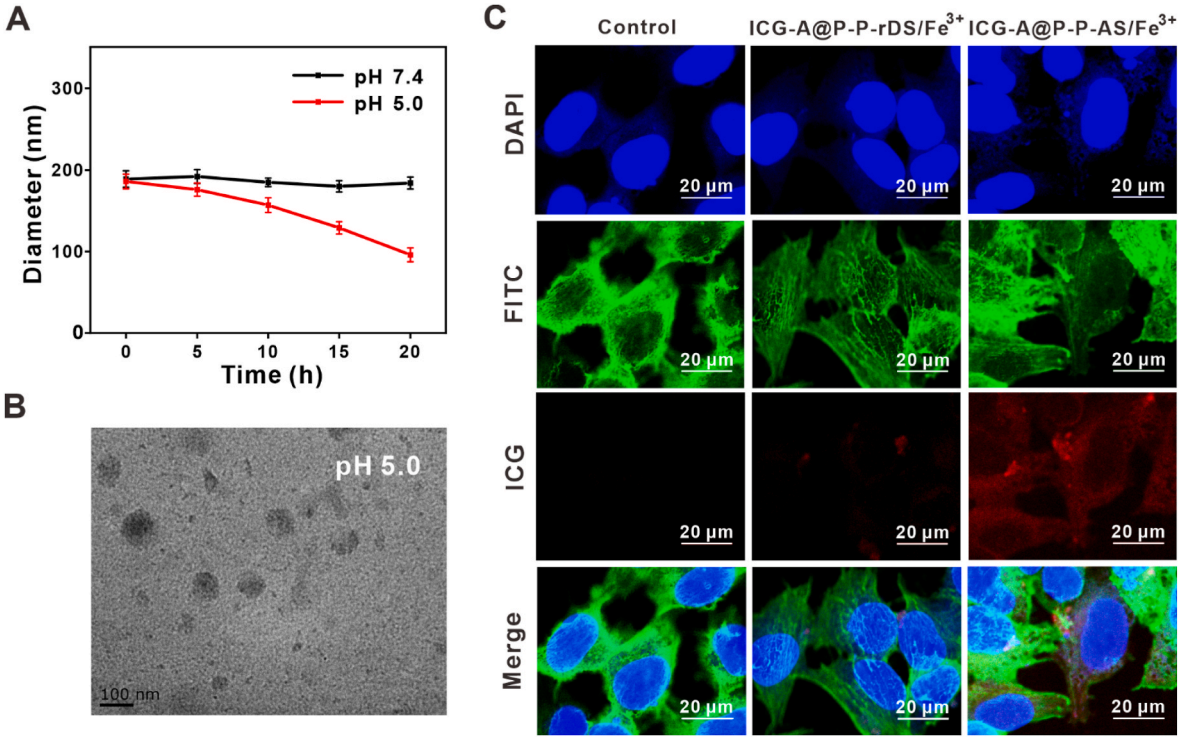

Fig. 3. Releasing and cellular uptake of A@P–P-AS/Fe^{3+}. (A) Hydrodynamic diameters of A@P–P-AS/Fe^{3+} under the condition of pH 7.4 or pH 5.0 every 5 h with time. (n = 3) (B) TEM image of A@P–P-AS/Fe^{3+} under the condition of pH 5.0. Scale bar: 100 nm. (C) Representative confocal fluorescence micrographs of SK-N-BE (2) cells with their nucleus (blue), cytoskeleton (green) and the ICG (red) stained. Scale bars: 20 μm. (For interpretation of the references to color in this figure legend, the reader is referred to the Web version of this article.)

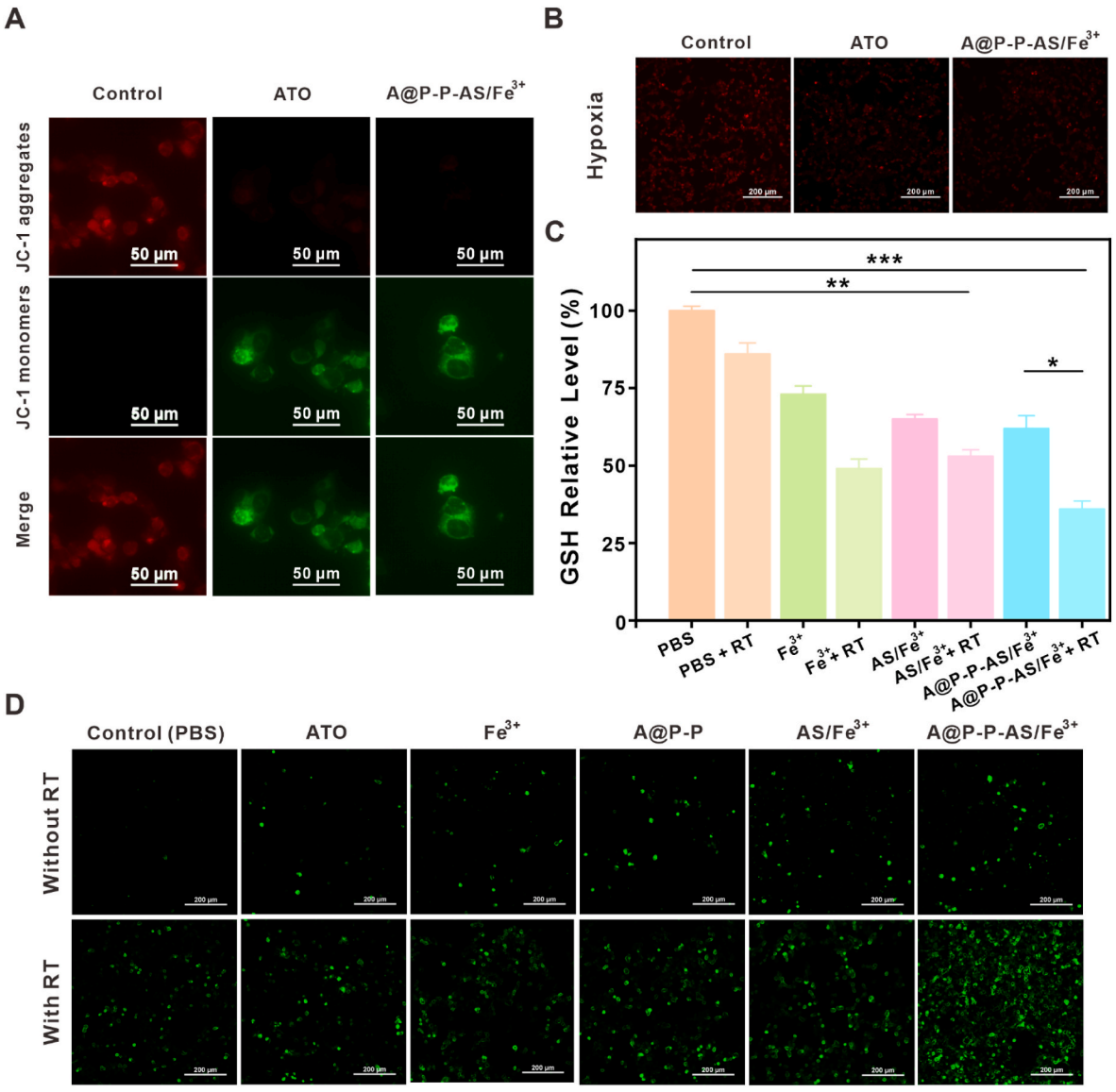

Fig. 4. Two parallel free radicals-amplifying pathways of A@P–P-AS/Fe^{3+}. (A) Fluorescence images of SK-N-BE (2) cells with JC-1 aggregates (red) and JC-1 monomers (green) in different treatments. Scale bars: 50 μm. (B) Fluorescence micrographs analysis results of SK-N-BE (2) cells incubated with hypoxia probes after diverse treatments. Scale bars: 200 μm. (C) GSH relative levels compared with the control (PBS) group in SK-N-BE (2) cells with diverse treatments. n = 3, *: $P < 0.05$; **: $P < 0.01$; ***: $P < 0.001$. (D) ROS generation of SK-N-BE (2) cells with diverse treatments detected by DCFH-DA. Scale bars: 200 μm. (For interpretation of the references to color in this figure legend, the reader is referred to the Web version of this article.)

consumption (Fig. 4B). Moreover, the intracellular GSH level was detected by DTNB (used to quantify the concentration of hydrosulphonyl [34]) after diverse treatments. Fig. 4C revealed that Fe^{3+} successfully diminished the intracellular GSH level in the SK-N-BE (2) cells during RT. With respect to the control cells, the intracellular level of GSH declined remarkably in A@P–P-AS/Fe^{3+} group with RT. Furthermore, DCFH-DA, free-radical probes, was used to detect the intracellular ROS level by producing green fluorescence. As shown in Fig. 4D, compared with the control group, A@P–P-AS/Fe^{3+} noticeably promoted the generation of ROS during the treatment of LDRT (1.5 Gy/10 min per 12 h, 3 Gy in total). These results demonstrated that A@P–P-AS/Fe^{3+} mitigated hypoxia and attenuated the antioxidant capability of the SK-N-BE (2) cells, which would enhance ROS production and amplify the antitumor effect of LDRT [35].

3.3. *In vitro antitumor activity*

To evaluate the antitumor effect of A@P–P-AS/Fe^{3+} in vitro, Cell viability assay was used to investigate the cytotoxicity of different treatments with or without LDRT. The groups treated with PBS and PBS plus LDRT were set as controls. The results showed little cytotoxicity of A@P–P-AS/Fe^{3+} alone to the SK-N-BE (2) cells while strong synergistic cytotoxicity of A@P–P-AS/Fe^{3+} to the SK-N-BE (2) cells with LDRT in contrast with control groups (Fig. 5A). Additionally, half maximal inhibitory concentration (IC_{50}) of A@P–P-AS/Fe^{3+} was about 1.8 μg/mL with LDRT (Fig. S7). In order to visually estimate the antitumor efficiency of A@P–P-AS/Fe^{3+} in vitro, Live/Dead cells staining assay was performed and as expected, under the LDRT most SK-N-BE (2) cells treated with A@P–P-AS/Fe^{3+} were dead and showed intensive red fluorescence (Fig. 5B). Besides, it also revealed that A@P–P-AS/Fe^{3+} plus LDRT led to more tumor cell death with the ability of dual-channel parallel ROS-generating enhancement comparing to the group of A@P–P plus LDRT or AS/Fe^{3+} plus LDRT which were capable of singer-channel ROS-generating enhancement. It showed similar results in flowcytometry analysis of apoptosis. A@P–P-AS/Fe^{3+} plus LDRT induced more SK-N-BE (2) cells into apoptosis in comparison with the

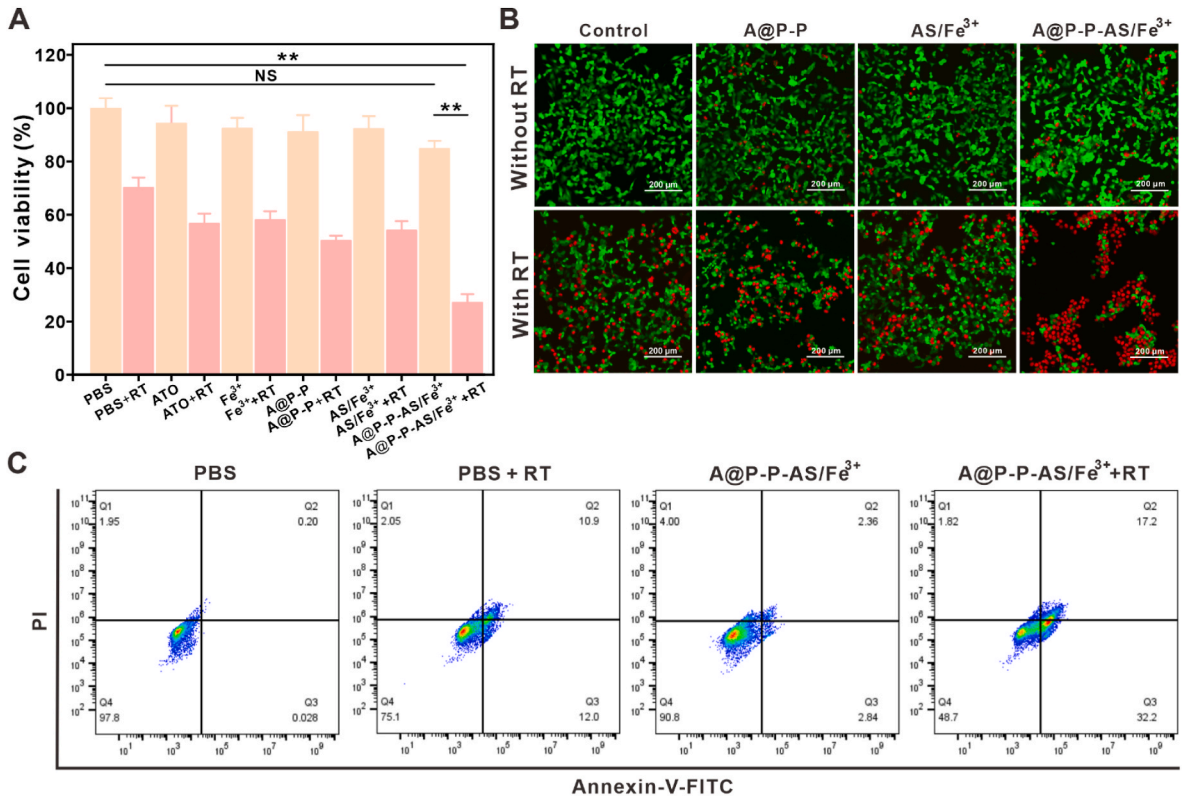

Fig. 5. Antitumor effect of A@P–P-AS/Fe^{3+} in vitro. (A) Cell viability of the SK-N-BE (2) cells after diverse treatments. (n = 4), NS: No Significance; **: $P < 0.01$. (B) Fluorescence micrographs of the SK-N-BE (2) cells co-stained with Nuclei Dye (red) and Live Dye (green) after various treatments. Scale bars: 200 μm. (C) Flow cytometry analysis of apoptosis and necrosis of cells treated with different treatments. (For interpretation of the references to color in this figure legend, the reader is referred to the Web version of this article.)

control groups (Fig. 5C), agreeing with the remarkable amplification of sensitization by A@P–P-AS/Fe^{3+} during LDRT.

3.4. *In vivo therapeutic efficacy*

To examine the targeting ability of A@P–P-AS/Fe^{3+} in vivo, ICG was packaged into the core, serving as the visualized marker of the nano-amplifier. Tumor-bearing mice were intravenously injected with the groups of PBS + ICG (control), ICG-A@P–P-rDS/Fe^{3+} (rDS, random DNA sequence, without targeting ability), and ICG-A@P–P-AS/Fe^{3+} (AS, AS1411, with targeting ability), and the fluorescence signal of ICG was investigated by the In Vivo Imaging System. As shown in Figs. S8 and S9, we found that ICG-A@P–P-AS/Fe^{3+} significantly accumulated in the tumor site compared with the ICG-A@P–P-rDS/Fe^{3+} and the control group. And the accumulation of the nanoparticles at the tumor site would meet the maximum at 24 h post-injection (Fig. S10). In order to assess whether A@P–P-AS/Fe^{3+} would strengthen the sensitization of neuroblastoma to LDRT, we further studied the synergistic therapeutic efficacy of A@P–P-AS/Fe^{3+} with LDRT in BALB/c mice bearing subcutaneous SK-N-BE (2) tumors. When the tumors developed to about 150 mm^3, tumor-bearing mice were intravenously injected with the groups of PBS, P–P-AS/Fe^{3+} (with the ability to reduce overexpressed GSH in tumor), A@P–P-AS (with the ability to improve tumor hypoxia micro-environment) or A@P–P-AS/Fe^{3+} (with the ability to reduce overexpressed GSH in tumor and improve tumor hypoxia microenvironment). Then, the mice above were irradiated with LDRT or not at 24 h post-injection (Fig. S10). As displayed in Fig. 6A, the mice treated with PBS or PBS plus LDRT showed rapid tumor growth in the similar way, revealing that LDRT alone had no noticeable therapeutic benefits to the tumors. And the groups with P–P-AS/Fe^{3+} or A@P–P-AS had only a slight enhancement to the LDRT owing to the singer-channel ROS-generating stimulation. While the size of SK-N-BE (2) tumors were remarkably scaled down by the A@P–P-AS/Fe^{3+} plus LDRT in contrast to the groups above, which demonstrated that the dual-channel parallel radicals nanoamplifier A@P–P-AS/Fe^{3+} could effectively enhance the therapeutic efficacy of LDRT and suppress tumor growth (Fig. 6A and C). Besides, the level of GSH in tumor after treated with A@P–P-AS/Fe^{3+} plus LDRT was evidently lower than that with PBS or LDRT alone (Fig. 6D), which may be attributable to the counteraction of intracellular antioxidant capacity by A@P–P-AS/Fe^{3+}. Moreover, compared with other groups, A@P–P-AS/Fe^{3+} with RT showed most intense oxidative stress in tumor (Fig. S11). That is to say, combining with the results in vitro, the consumption of GSH by A@P–P-AS/Fe^{3+} may increase the accumulation of ROS during the LDRT, leading to more oxidative stress damage to tumor cells. To confirm the DNA breaks in SK-N-BE (2) tumor cells after different treatments, we performed immunofluorescence assay with γ-H2AX (specific marker to the DNA breaks) to visualize the profile of breaking DNA in tumor cells. As shown in Fig. 6F, compared with other groups, the treatment of A@P–P-AS/Fe^{3+} plus LDRT enhanced the level of DNA breaks most remarkably. Additionally, HE, TUNEL and Ki-67 staining were utilized to investigated tumor morphology, cell death and cell vitality. As proved in Fig. 6E, G and H, the group of A@P–P-AS/Fe^{3+} plus LDRT illustrated a large area of cell necrosis and lower cell proliferation activity, proving that A@P–P-AS/Fe^{3+} plus LDRT could substantially inhibit the propagation of SK-N-BE (2) tumors. Semi-quantitative analysis of the immunohistochemical staining above was shown in Figs. S12 and S13. This result was consistent with the result in vitro. Besides, the antitumor activity of ATO, Fe^{3+} or A@P–P-AS/Fe^{3+} without LDRT in vivo was also evaluated (n = 5). However, compared with the control group (PBS), there was no significant difference in tumor volume during 2 weeks with the treatments of A@P–P-AS/Fe^{3+}, A@P–P or AS/Fe^{3+} alone (n = 5) (Fig. S14A). It

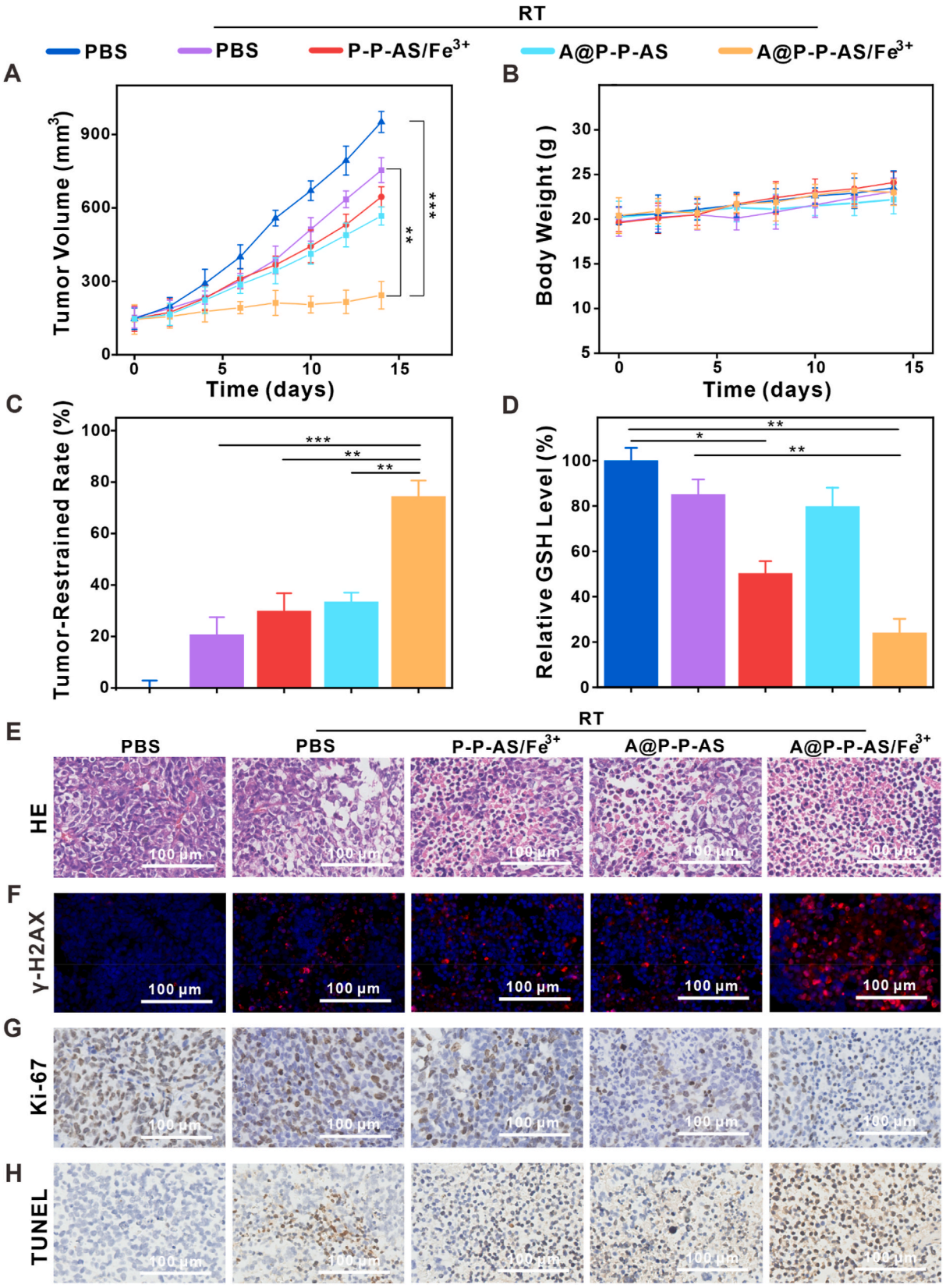

Fig. 6. In Vivo Therapeutic Efficacy of A@P–P-AS/Fe^{3+}. (A) Tumor growth curves of SK-N-BE (2) tumor-bearing mice in different groups. (n = 5) (B) Body weight of mice with different treatments. (C) Tumor-restrained rates curves of tumor growth with diverse treatments. (D) In vivo relative GSH levels of SK-N-BE (2) tumor after different treatments. (E, F, G and H) HE, γ-H2AX, Ki-67 and TUNEL staining of SK-N-BE (2) tumor sections after treatments in different groups. *: $P < 0.05$; **: $P < 0.01$; ***: $P < 0.001$. Scale bars: 100 μm.

showed similar results in HE, Ki-67 and TUNEL staining (Fig. S14B). Since the antitumor activity of A@P–P-AS/Fe^{3+} without LDRT was similar to the PBS, we confirmed that the tumor killing capacity of A@P–P-AS/Fe^{3+} must be initiated by radiotherapy.

It's essential to estimate the potential toxic side effect of A@P–P-AS/Fe^{3+} treatment with or without LDRT. Hemolysis of A@P–P-AS/Fe^{3+} in different concentration (Fig. S15) showed that even high concentration of A@P–P-AS/Fe^{3+} would merely cause almost undetected hemolysis. In addition, We assessed the blood half-life of A@P–P-AS/Fe^{3+}, which was approximately 223 min (Fig. S16). And we regarded the loss of body weight as the indicator for treatment-induced toxicity. As Fig. 6B showed, there was no significant body weight variation in the mice after diverse treatments. Moreover, the potential toxicity of the treatments to main organs including heart, liver, spleen, lung and kidneys of all five groups mice was evaluated by HE staining, which indicated no obvious damage 15 days after the treatment with A@P–P-AS/Fe^{3+} plus LDRT (Fig. S17). These data testified to the dual-channel parallel radicals nanoamplifier A@P–P-AS/Fe^{3+}-empowered enhancement of LDRT to SK-N-BE (2) tumors in vivo while causing little adverse effect.

4. Conclusion

In this study, we developed a low-dose radiosensitization approach for improving the sensitivity of neuroblastoma to RT by the construction of a dual-channel parallel free radicals nanoamplifier (A@P–P-AS/Fe^{3+}). Compared to most of previously reported oxygen free radicals-based radiosensitization, this approach possesses two parallel free radicals-amplifying pathways: 1) ATO can remarkably limit the oxygen consumption of mitochondrial respiration, alleviating tumor hypoxia-confined radiosensitization and invoking the first free radicals-amplifying pathway; 2) the redox between Fe^{3+} and GSH significantly decreases the GSH level in tumor cells, which successfully avoids the large scavenging of the generated free radicals and contributes to the second free radicals-amplifying pathway. Collectively, we envision this technology has a promising potential in revolutionizing the current landscape of low-dose RT in neuroblastoma or other solid tumors.

Credit author statement

Wenxin Zhang: Conceptualization, Investigation, Methodology, Validation, Software, Writing-original draft. Xiaodie Li: Software, Investigation, Methodology. Jialin Zeng: Investigation, Software, Visualization. Xin Wen: Software, Methodology. Chao Zhang: Funding acquisition, Resources, Visualization. Yinan Zhang: Funding acquisition, Project administration, Supervision. Jian He: Conceptualization, Methodology, Project administration, Supervision. Lihua Yang: Project administration, Resources, Supervision, Validation, Writing-review & editing.

Declaration of competing interest

The authors declare that they have no known competing financial interests or personal relationships that could have appeared to influence the work reported in this paper.

Data availability

Data will be made available on request.

Acknowledgments

The authors thank the financial support of the National Natural Science Foundation of China (No. 22207085), the Fundamental Research Funds for the Central Universities (No. 22120230236), Guangdong Basic and Applied Basic Research Foundation (No. 2022A1515110845, No. 2023A1515011042), Science and Technology Program of Guangzhou (No. 2023A04J0060).

Appendix A. Supplementary data

Supplementary data to this article can be found online at https://doi.org/10.1016/j.mtbio.2023.100828.

References

[1] K.K. Matthay, J.M. Maris, G. Schleiermacher, A. Nakagawara, C.L. Mackall, L. Diller, W.A. Weiss, Neuroblastoma, Nat. Rev. Dis. Primers 2 (2016), 16078.
[2] B. Qiu, K.K. Matthay, Advancing therapy for neuroblastoma, Nat. Rev. Clin. Oncol. 19 (8) (2022) 515–533.
[3] R.L. Siegel, K.D. Miller, H.E. Fuchs, A. Jemal, Cancer statistics, 2021, CA A Cancer J. Clin. 71 (1) (2021) 7–33.
[4] N.J. Skertich, F. Chu, I.A.M. Tarhoni, S. Szajek, M.B. Madonna, Expression of immunomodulatory checkpoint molecules in drug-resistant neuroblastoma: an exploratory study, Cancers 14 (3) (2022).
[5] J.M. Maris, Recent advances in neuroblastoma, N. Engl. J. Med. 362 (23) (2010) 2202–2211.
[6] R. Nguyen, C.J. Thiele, Immunotherapy approaches targeting neuroblastoma, Curr. Opin. Pediatr. 33 (1) (2021) 19–25.
[7] D. Schaue, W.H. McBride, Opportunities and challenges of radiotherapy for treating cancer, Nat. Rev. Clin. Oncol. 12 (9) (2015) 527–540.
[8] H.G. Gatcombe, R.B. Marcus Jr., H.M. Katzenstein, M. Tighiouart, N. Esiashvili, Excellent local control from radiation therapy for high-risk neuroblastoma, Int. J. Radiat. Oncol. Biol. Phys. 74 (5) (2009) 1549–1554.
[9] D.A. Haas-Kogan, P.S. Swift, M. Selch, G.M. Haase, R.C. Seeger, R.B. Gerbing, Impact of radiotherapy for high-risk neuroblastoma: a Children's Cancer Group study, Int. J. Radiat. Oncol. Biol. Phys. 56 (1) (2003) 28–39.
[10] D.L. Casey, B.H. Kushner, N.V. Cheung, S. Modak, M.P. LaQuaglia, Dose-escalation is needed for gross disease in high-risk neuroblastoma, Pediatr, Blood Cancer 65 (7) (2018), e27009.
[11] D.L. Casey, B.H. Kushner, N.K. Cheung, S. Modak, M.P. LaQuaglia, Local control with 21-gy radiation therapy for high-risk neuroblastoma, Int. J. Radiat. Oncol. Biol. Phys. 96 (2) (2016) 393–400.
[12] Q. Li, J. Wang, Y. Cheng, A. Hu, D. Li, X. Wang, Y. Guo, Y. Zhou, G. Chen, B. Bao, Long-term survival of neuroblastoma patients receiving surgery, chemotherapy, and radiotherapy: a propensity score matching study, J. Clin. Med. 12 (3) (2023).
[13] B.H. Kushner, S. Wolden, M.P. LaQuaglia, K. Kramer, D. Verbel, G. Heller, N. K. Cheung, Hyperfractionated low-dose radiotherapy for high-risk neuroblastoma after intensive chemotherapy and surgery, J. Clin. Oncol. 19 (11) (2001) 2821–2828.
[14] K.X. Liu, A. Naranjo, F.F. Zhang, S.G. bDuBois, S.E. Braunstein, S.D. Voss, G. Khanna, W.B. London, J.J. Doski, J.D. Geiger, Prospective evaluation of radiation dose escalation in patients with high-risk neuroblastoma and gross residual disease after surgery: a report from the children's oncology group ANBL0532 study, J. Clin. Oncol. 38 (24) (2020) 2741–2752.
[15] L. Gong, Y. Zhang, C. Liu, M. Zhang, S. Han, Application of radiosensitizers in cancer radiotherapy, Int. J. Nanomed. 16 (2021) 1083–1102.
[16] L. Galluzzi, I. Vitale, S.A. Aaronson, J.M. Abrams, D. Adam, P. Agostinis, E. S. Alnemri, L. Altucci, I. Amelio, D.W. Andrews, Molecular mechanisms of cell death: recommendations of the nomenclature committee on cell death 2018, Cell Death Differ. 25 (3) (2018) 486–541.
[17] P.G. Pilié, C. Tang, G. B Mills, T.A. Yap, State-of-the-art strategies for targeting the DNA damage response in cancer, Nat. Rev. Clin. Oncol. 16 (2) (2019) 81–104.
[18] H. Wang, X. Mu, H. He, X.D. Zhang, Cancer radiosensitizers, Trends Pharmacol. Sci. 39 (1) (2018) 24–48.
[19] C. Huertas-Castano, M.A. Gomez-Munoz, M. Bpardal, R.F. Vega, Hypoxia in the initiation and progression of neuroblastoma tumours, Int. J. Mol. Sci. 21 (1) (2019).
[20] Y. Xiong, C. Xiao, Z. Li, X. Yang, Engineering nanomedicine for glutathione depletion-augmented cancer therapy, Chem. Soc. Rev. 50 (10) (2021) 6013–6041.
[21] D. Tao, L. Feng, Y. Chao, C. Liang, X. Song, H. Wang, K. Yang, Z. Liu, Covalent organic polymers based on fluorinated porphyrin as oxygen nanoshuttles for tumor hypoxia relief and enhanced photodynamic therapy, Adv. Funct. Mater. 28 (43) (2018).
[22] T.Y. Yen, Z. R Stephen, G. Lin, Q. Mu, M. Jeon, S. Untoro, P. Welsh, M. Zhang, Catalase-functionalized iron oxide nanoparticles reverse hypoxia-induced chemotherapeutic resistance, Adv. Healthcare Mater. 8 (20) (2019), e1900826.
[23] H. Zhou, Z. Fan, J. Deng, P.K. Lemons, D.C. Arhontoulis, W.B. Bowne, H. Cheng, Hyaluronidase embedded in nanocarrier PEG shell for enhanced tumor penetration and highly efficient antitumor efficacy, Nano Lett. 16 (5) (2016) 3268–3277.
[24] X. Mai, Y. Zhang, H. Fan, W. Song, Y. Chang, B. Chen, J. Shi, X. Xin, Z. Teng, Integration of immunogenic activation and immunosuppressive reversion using mitochondrial-respiration-inhibited platelet-mimicking nanoparticles, Biomaterials 232 (2020), 119699.
[25] W. Yu, T. Liu, M. Zhang, Z. Wang, J. Ye, C.X. Li, W. Liu, R. Li, O_2 economizer for inhibiting cell respiration to combat the hypoxia obstacle in tumor treatments, ACS Nano 13 (2) (2019) 1784–1794.
[26] D. Xia, P. Xu, X. Luo, J. Zhu, H. Gu, D. Huo, Y. Hu, Overcoming hypoxia by multistage nanoparticle delivery system to inhibit mitochondrial respiration for photodynamic therapy, Adv. Healthcare Mater. 29 (13) (2019).

[27] D. Smilowicz, F. Kogelheide, K. Stapelmann, P. Awakowicz, N. Metzler-Nolte, Study on chemical modifications of glutathione by cold atmospheric pressure plasma (cap) operated in air in the presence of Fe(II) and Fe(III) complexes, Sci. Rep. 9 (1) (2019), 18024.
[28] X. Huang, W. Liao, G. Zhang, S. Kang, C.Y. Zhang, pH-sensitive micelles self-assembled from polymer brush (PAE-g-cholesterol)-b-PEG-b-(PAE-g-cholesterol) for anticancer drug delivery and controlled release, Int. J. Nanomed. 12 (2017) 2215–2226.
[29] X. Tong, L. Ga, J. Ai, Y. Wang, Progress in cancer drug delivery based on AS1411 oriented nanomaterials, J. Nanobiotechnol. 20 (1) (2022) 57.
[30] R. Yazdian-Robati, P. Bayat, F. Oroojalian, M. Zargari, M. Ramezani, S.M. Taghdisi, K. Abnous, Therapeutic applications of AS1411 aptamer, an update review, Int. J. Biol. Macromol. 155 (2020) 1420–1431.
[31] S. Li, Q. Jiang, S. Liu, Y. Zhang, Y. Tian, A DNA nanorobot functions as a cancer therapeutic in response to a molecular trigger in vivo, Nat. Biotechnol. 36 (3) (2018) 258–264.
[32] M.M. Kim, A.A. Ghogare, A. Greer, T.C. Zhu, On the in vivo photochemical rate parameters for PDT reactive oxygen species modeling, Phys. Med. Biol. 62 (5) (2017) R1–r48.
[33] J. Wang, W. Liu, G. Luo, Z. Li, C. Zhao, H. Zhang, M. Zhu, Q. Xu, X. Wang, Synergistic effect of well-defined dual sites boosting the oxygen reduction reaction, Energy Environ. Sci. 11 (12) (2018) 3375–3379.
[34] I. Rahman, A. Kode, S.K. Biswas, Assay for quantitative determination of glutathione and glutathione disulfide levels using enzymatic recycling method, Nat. Protoc. 1 (6) (2006) 3159–3165.
[35] P. Liu, L. Hao, M. Liu, S. Hu, Glutathione-responsive and -exhausting metal nanomedicines for robust synergistic cancer therapy, Front. Bioeng. Biotechnol. 11 (2023), 1161472.